Curtailing Perovskite Processing Limitations via Lamination at the Perovskite/Perovskite Interface

*Sean P. Dunfield[1,2,3], David T. Moore[1], Talysa R. Klein[1], David M. Fabian[1,6], Jeffrey A. Christians[1], Alex G. Dixon[1,2], Benjia Dou[1,5], Shane Ardo[6,7], Matthew C. Beard[1], Sean E. Shaheen[2,4,5], Joseph J. Berry[1,2,4 *], Maikel F.A.M. van Hest[1,*]*

National Renewable Energy Laboratory, Golden, CO 80401[1]

Renewable and Sustainable Energy Institute, University of Colorado Boulder, Boulder, CO 80309[2]

Materials Science & Engineering Program, University of Colorado Boulder, Boulder, CO 80309[3]

Department of Physics, University of Colorado Boulder, Boulder, CO 80309[4]

Department of Electrical, Computer and Energy Engineering, University of Colorado Boulder, Boulder, CO 80309[5]

Department of Chemistry, University of California Irvine, Irvine, CA 92697[6]

Department of Chemical Engineering and Materials Science, University of California Irvine, Irvine, CA 92697[7]

Corresponding Authors*: maikel.van.hest@nrel.gov, joe.berry@nrel.gov

Standard layer-by-layer solution processing methods constrain lead–halide perovskite device architectures, as the layer below the perovskite must be robust to the strong organic solvents used to form the perovskite, while the layer above has a limited thermal budget and must be processed in non-polar solvents to prevent perovskite degradation. To circumvent these limitations, we develop a procedure where two transparent conductive oxide/transport material/perovskite half stacks are independently fabricated and then laminated together at the perovskite–perovskite interface. Using UV-visible absorption spectroscopy, external quantum efficiency, X-ray diffraction, and time-resolved photoluminesence spectroscopy, we show that this procedure improves properties of the perovskite layer. Applying this procedure, semi-transparent devices employing two high-temperature oxide transport layers were fabricated, which realize an average efficiency of 9.6% (maximum: 10.6%) despite series resistance limitations from the substrate design. Overall, the developed lamination procedure curtails processing constraints, enables new device designs, and affords new opportunities for optimization.

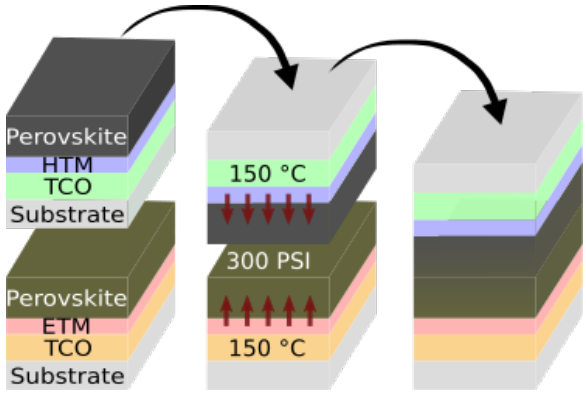

Since emerging as a viable material for use in photovoltaic devices in 2009, lead–halide perovskites have attracted an enormous amount of attention due to their near-ideal photovoltaic properties[1] and low-temperature solution-based fabrication.[2,3] Process and composition optimization has spearheaded advancements in material stability[4] and led to an unprecedented rise in efficiency from 3.8%[5] to 22.6%[6] in just eight years. Despite their excellent performance, many aspects of these devices need further investigation due to the complex interplay between the perovskite layer and other device material layers that impacts the details of their formation[7–10] and resulting device behavior.[11,12] Gaining a fundamental understanding of these matters will be essential in progressing from material stability to device stability and reducing non-radiative losses in photovoltage.[13,14] Nonetheless, these topics have not been adequately studied, in large part because standard solution deposition methods[15,16] create solvent compatibility issues and thermal budgeting constraints that limit the materials and architectures that can be applied in devices; for example, most metal oxides cannot be deposited on top of the perovskite layer using conventional solution processing.[17] The use of a lamination procedure in which two independently-processed perovskite half stacks are laminated together circumvents a number of these process limitations and can be applied to a wide range of materials used in perovskite optoelectronic devices.[18] This work focuses on the development of such a lamination procedure, evaluation of its impact on the structural, optical, photophysical, and electronic properties of the perovskite layer, and demonstration of its ability to produce functioning devices. To establish and optimize processing conditions, a tin oxide (SnO_x) electron transport material (ETM), nickel oxide (NiO_x) hole transport material (HTM), fluorine-doped tin oxide (FTO) coated glass substrates, and two methylammonium lead triiodide ($CH_3NH_3PbI_3$, MAPI) perovskite active layers are utilized.

Due to the complex interplay between the perovskite and other device material layers, minor changes in substrate preparation, solution stoichiometry, deposition parameters, and annealing conditions have been shown to alter film formation and composition,[9,19–22] such as the amount of lead iodide (PbI_2) present in films. Using the $CH_3NH_3PbI_3$ (100) and PbI_2 (001) peak area ratios obtained from powder X-ray diffraction (XRD), the ratio of $CH_3NH_3PbI_3$-to-PbI_2 in each half stack was maximized so that the presence of PbI_2 could be used as an indicator of the following thermal degradation pathway[22–26] in laminated devices:

$$CH_3NH_3PbI_3\,(s) + \text{heat} \rightleftharpoons CH_3NH_2\,(g) + HI\,(g) + PbI_2\,(s) \qquad \text{(Equation 1)}$$

Note that while the reaction above is reversible and occurs at temperatures as low as 100 °C, two of the three reaction products are capable of off-gassing in standard geometry, driving the reaction forward as predicted by Le Chatelier's Principle. In contrast, the lamination process utilized here should encapsulate the products ~~gases~~ formed in thermal decomposition between the two glass substrates, balancing Equation 1 and preventing it from proceeding. By forming a smooth charge transport layer, utilizing a MAPI solution with an optimized MAI to PbI_2 ratio, and annealing the resulting perovskite for at least 15 minutes at 100 °C, MAPI films with little to no PbI_2 were sucessfully produced on both SnO_x and NiO_x (Figure 1). These films should be ideal for lamination, as the formulation utilized is known to produce films with

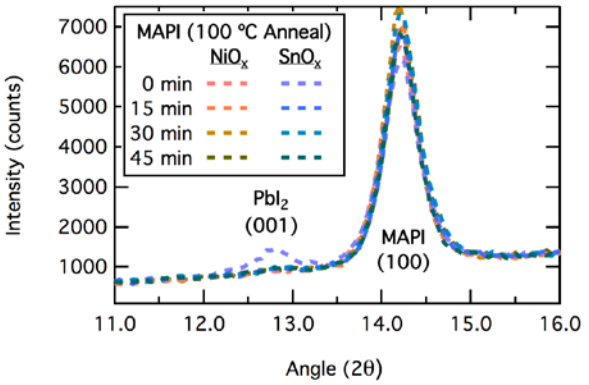

Figure 1. PbI_2 (001) [2θ = 12.8°] and MAPI (100) [2θ = 14.2°] XRD peaks for MAPI thin films on smooth SnO_x and NiO_x as a function of perovskite annealing time.

low surface roughness.[16] Additionally, these films are of high quality, as evidenced by their performance in standard device architectures (Figure S5).

Once optimized, the half stacks were laminated together using a hot press at ~300 psi and 150 °C for 20 min as described in the Supplementary Information (SI). To gauge the effect of lamination on the perovskite active layer, a series of analyses were conducted including UV-visible absorption spectroscopy, external quantum efficiency (EQE), XRD, and time-resolved photoluminesence spectroscopy (TRPL).

Absorption spectra were obtained for FTO/SnO_x-or-NiO_x/MAPI half stacks, laminated samples, delaminated samples, and FTO/SnO_x-or-NiO_x references using the transmission and reflection spectra calculated from data acquired using an integrating sphere. To account for varying perovskite and glass thickness while maintaining the shape and location of the band edge, curves were linearly normalized as described in the SI. As shown in Figure 2a, the absorption data indicates that lamination decreases the band gap of the perovskite and maintains or sharpens the features at the absorption band edge, corresponding to a modification of the conduction and/or valence band edge structures and associated defects.[27] Subsequent delamination at the SnO_x/MAPI interface (described in the SI) appears to further reduce the band gap of the perovskite and partially revert the shape of the band edge back to its pre-laminated form. Consequently, delaminated samples should serve as a reasonable qualitative metric for the effects of lamination.

Changes in absorption were confirmed using EQE measurements on a FTO/SnO_x/laminated MAPI/NiO_x/FTO device and a control FTO/SnO_x/MAPI/Spiro-OMeTAD/MoO_x/Al device fabricated without lamination as described in the SI. To compare the shape of the EQE band edges, spectra were again normalized as above. The red shift measured with EQE, shown in

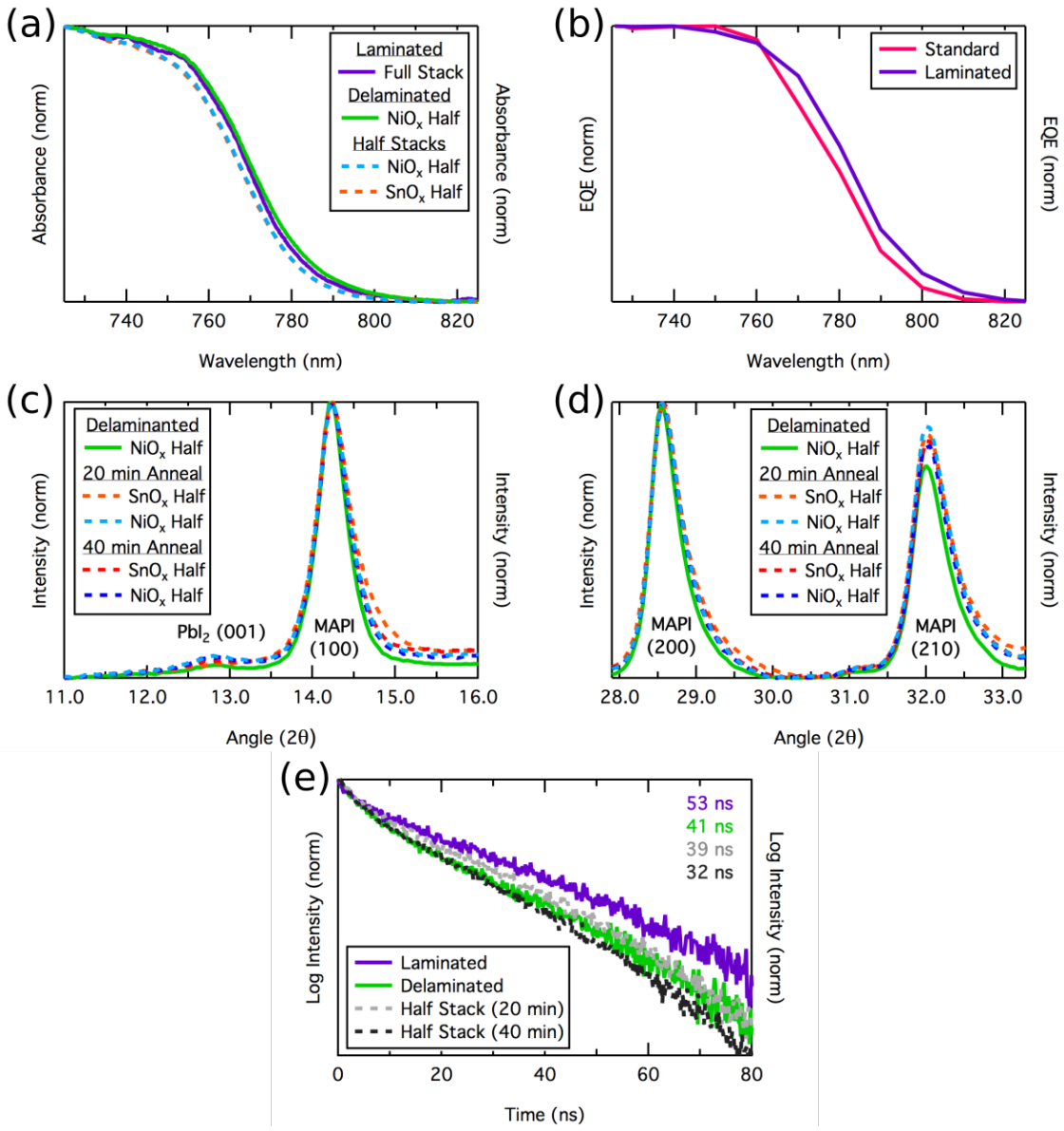

Figure 2. Characterization of pre-laminated half stacks, laminated stacks, and delaminated stacks used to gauge the effects of lamination including: (a) absorbance spectroscopy, (b) external quantum efficiency, (c) X-ray diffraction of PbI2 (001) and MAPI (100) peaks, (d) X-ray diffraction of MAPI (200) and (210) peaks, and (e) time-resolved photoluminescence spectroscopy.

Figure 2b, agrees with that of the absorption measurements within the resolution of the instrument (~5 nm). To ascertain what extent the changes in the optical spectra correlate to structural changes induced by the lamination process, pre-laminated half stacks fabricated with typical annealing conditons, pre-laminated half stacks with additional thermal annealing, and delaminated half stacks were analyzed via XRD. Results, shown normalized to the most intense peak for clarity in Figure 2c and 2d, display three main trends for the laminated devices: a decrease in the full width at half maximum of all peaks attributed to MAPI, an increase in the MAPI (200)-to-MAPI (210) ratio, and an invariance in the PbI_2 (001)-to-MAPI (100) ratio. Note that improvements of similar magnitude are not seen in devices with additional thermal input. This suggests that something particular afforded by lamination and successive delamination results in increased crystallinity and an orientation of domains to favor the (100) crystal orientiation with no detectable thermal decomposition. Although measured on delaminated stacks, the results are consistent with other measurements, providing evidence that changes to the electronic structure arise in part by a change in morphology.

To correlate these optical and morphological changes to a functional property of the photovoltage, time-resolved photoluminesence spectroscopy was conducted on glass/MAPI samples, glass/laminated MAPI/glass samples, and glass/delaminated MAPI samples. As lifetimes are known to correlate with excitation intensity,[28] analysis was conducted using 450 nm wavelength excitation through the glass face of each sample with constant excitation fluence. While the glass backside of the laminated sample certainly results in varied amounts of attenuation and scattering, all perturbations were intensity-independent and therefore should not affect lifetime. Despite optimal sample orientation and constant fluance, variations in the density of free charge carriers generated during excitation are expected due to the differences observed

in absorption. Although lifetimes at shorter time scales are heavily perturbed by complex free-carrier density-dependent effects, such as band gap renormalization[29] and bimolecular recombination[30], longer time scales where trap-mediated recombination processes dominate recombination kinetics are expected to have smaller intensity dependence. Consequently, the logarithm of the intensity is highly linear after the initial several nanosecconds as shown in Figure 2e. To account for this, data was truncated for fitting to exclude points prior to 20 ns, such that a single-exponential fit produces small residuals (see SI). Consistent with the hypothesis that lamination improves the electronic structure and reduces defects/traps within the perovskite layer~~, The~~ results show that~~, consistent with the hypothesis that lamination improves the electronic structure and reduces defects/traps within the perovskite layer~~, laminated samples exhibit longer carrier lifetimes of ~53 ns, compared to ~41 ns for the delaminated device, ~39 ns for the pre-laminated device with normal thermal input, and ~32 ns for the pre-laminated device with additional thermal input. ~~Therefore, lamination appears to beneficially alter the material quality of the perovskite layer by likley reducing the concentration of defects/traps and improving the charge-carrier dynamics and morphological sturcture.~~

Together, the observed narrowing of the X-ray diffraction peaks, red shift of the absorption and external quantum efficiency data, and the increase in photoluminescence lifetime suggest that lamination beneficially alters the material quality of the perovskite layer, likley by reducing the concentration of defects/traps and improving the charge-carrier dynamics. Although the improvement in electronic properties is clear, further investigation is underway to ascertain what extent these improvements are due to better structure, stoichiometry, and passivation at the surfaces/interfaces.

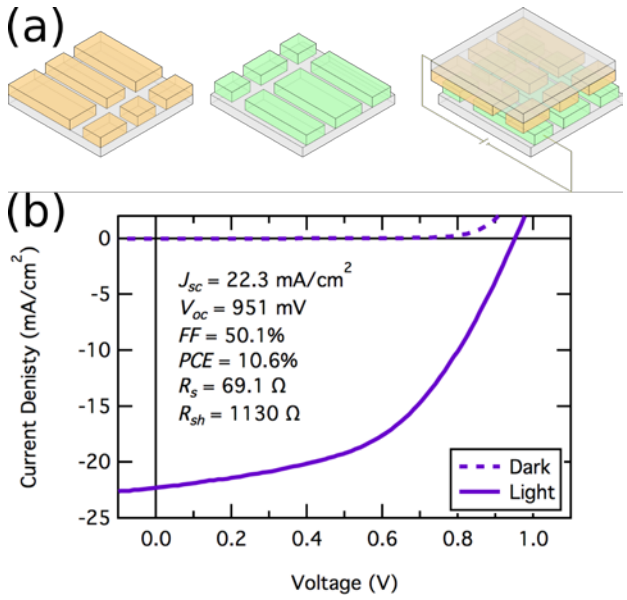

Figure 3. (a) Device TCO architecture utilized to create devices (b) and champion device *J–V* curve and corresponding parameters.

To demonstrate the newfound flexibility in device architectures afforded by lamination, devices which feature all-oxide transport layers (SnO_x/MAPI/NiO_x), an architecture that is generally inaccessable by conventional solution processing methods, were fabricated. A detailed optimization of substrate design and charge-transport layers was beyond the scope of this study; therefore, a simple substrate design (shown qualitatively in Figure 3a and with dimensions in the SI) was adopted. TEC 15 FTO substrates were patterned via laser scribing, coated with either NiO_x or SnO_x and perovskite, and laminated as described in the SI, resulting in ~25 mm^2 semi-transparent devices with a non-optimal ~800 nm thick MAPI active layer. The average device demonstrated a power conversion efficiency (PCE*)* of 9.6%, open-circuit voltage (V_{oc}) of 950 mV, short-circuit current density (J_{sc}) of 20.2 mA/cm^2, fill factor (FF) of 50.0 %, shunt resistance (R_{sh}) of 1044 Ω, and series resistance (R_s) of 59 Ω. The *J–V* curve and corresponding parameters of the champion device are shown in Figure 3b. While these devices realize PCEs that are not competitive with standard processing, the predominant efficiency loss can be attributed to the R_s (~59 Ω), which is much larger than that observed in devices that utilize a geometrically well-designed architecture (< 5 Ω). This high R_s, which is responsible for losses in measured voltage and thus has a detremental impact on the FF, is caused by the architecture utilized to facilitate the lamination

process rather than the impact of lamination on the active layer itself. Namely, the use of two offset substrates with TCO pads causes the extracted current to flow an extra distance of at least 7.5 mm through a 5.0 mm or 6.5 mm wide TCO on each side, where major resistive losses of ~40 Ω occur (15 Ω/Square). Reducing R_s by using thicker TCO layers, a shorter distance from the active area to charge collection area, bus bars, or another strategy should drastically improve the measured PCE.

It is evident that a combination of pressure and heat is capable of bonding the two perovskite thin films together. Devices made using this method perform at reasonable efficiency in the primitive device architecture implemented here and the absorption, EQE, XRD, and TRPL results all indicate slight improvements in properties of the laminated perovskite active layers, ~~even when compared to samples with additional thermal input at 100 °C.~~ These improvements are above and beyond those seen with additional thermal input at 100 °C. Additionally, they do not appear to be caused by pressure, as the pressure-induced red-shift documented in MAPI occurs at two orders of magnitude greater pressure (~0.18 GPa)[31] and is accompanied by changes in XRD patterns[32] that are not observed here. Noting that they ~~the improvements seen in lamination~~ appear similar to those reported for perovskites synthesized using covered-solvent annealing at 150 °C with excess MAI or MACl,[15,33] we presume that these enhancements are due in part to the prevention or slowing of the thermal decay pathway decribed by Equation 1, allowing the thermal budget to be increased without inducing degradation. This decoupling of the positive effects of annealing from the negative byproduct of thermally-induced degradation is not achievable in standard processing of devices containing MA-based perovskites because temperatures sufficient for grain growth[22] are also adequate to induce thermal degradation, forming PbI_2 and organic gases that off-gas to allow degradation to proceed. Although many

mechanisms reasonably explain the improved properties of laminated samples, based on literature and our observations, it seems likely that the additional thermal input provided by lamination is sufficient to (a) cause the mobile A- and X-site ions of the ABX_3 perovskite structure to inter-diffuse[34,35], improving the stoichiometry within the grain by moving impurities to the grain boundaries, and (b) to partially thermally decompose the perovskite through a reaction similar to Equation 1, volatilizing and trapping in gases capable of partially solvating the perovskite between the two impermeable glass slides. These organic gases then mediate the bonding of any AX and BX_2 impurities at the grain boundaries, increasing grain size and improving uniformity.[15,33]

This method is supported by the XRD results. Specifically, the thermal load provided by a 20 minute anneal at 150 °C should be sufficient to thermally decompose the perovskite and thus generate large amounts of PbI_2,[22–26] but the self-encapsulated format of lamination instead appears to improve crystallinity without any detectable increase in PbI_2. In order to further probe this, two half stacks were laminated together inside a butyl-rubber barrier at ~300 psi and 150 °C on the hot press for 5 days. While the edges of the substrate showed visible signs of thermal degradation, the interior, where gases cannot escape, remained uniform and black rather than turning yellow, indicating no significant decomposition to PbI_2. This suggests that the bulk of the MAPI material is intrinsically stable and off-gassing is required for typical thermal degradation pathways (e.g. Equation 1) to proceed.

We have demonstrated a low-pressure and solvent-free lamination process at the perovskite–perovskite interface. Using a combination of absorption, EQE, XRD, and TRPL techniques, it is shown that the developed lamination process developed marginally improves the electronic structure, reduces the number of defects, increases the crystallinity, and enhances the

photophysical properties of the perovskite layer. In addition to affording these improvements, the lamination platform demonstrated herein is attractive for enabling the integration of two completely new sets of devices: (1) devices less sensitive to the typical thermal budgeting and solvent compatibility constraints and (2) devices which utilize two different perovskite half stacks (e.g. MAPI and $CH_3NH_3PbBr_3$ or $CH(NH_2)_2PbI_3$) to form a perovskite–perovskite heterojunction or graded band gap. The former was demonstrated here to fabricate semi-transparent devices employing two high-temperature oxide transport layers, SnO_x and NiO_x, which yielded an average efficiency of 9.6% and a maximum efficiency of 10.6% despite series resistance limitations from the substrate design and device structure; the latter is outside the scope of this work. Moreover, once optimized, the lamination procedure developed could be ideal for creating a self-encapsulated module architecture because the two impermeable glass substrates provide barriers that exclude extrinsic chemical species known to degrade the cell and trap in components that, if off-gassed, would result in perovskite decomposition.[22–26] Finally, even in its nascent form, the method demonstrated herein can be employed to provide insight into the degradation of halide perovskite solar cells. This is particularly true for interfaces, as the independent processing of the two half stacks allows for each perovskite/charge transport material interface to be manipulated and analyzed independently prior to the formation of the complete solar cell. Combined with newfound access to device material combinations, this should allow for further investigation in areas such as the effect of alternate interfaces and transport materials and the discrepancy in efficiency between n–i–p and p–i–n architectures. Consequently, while optimization of the lamination device architecture is still required to yield devices of competitive efficiency, lamination provides a viable route moving forward to curtail

solvent incompatibility and thermal budgeting issues, and as such provides new opportunities for device optimization in conventional and semi-transparent configurations of interest in tandems.

ASSOCIATED CONTENT

Supporting Information. List of chemicals and solvents, detailed description of fabrication of half stacks (substrate preparation and design, NiO_x, SnO_x, MAPI), lamination/delamination procedure, analysis (UV-vis Absorption, EQE, XRD, TRPL, *J–V* Characterization), and control FTO/SnO_x/MAPI/Spiro-OMeTAD/Au device.

Notes. The authors declare no competing financial interest.

AUTHOR INFORMATION

Sean P. Dunfield: sean.dunfield@colorado.edu

Maikel F.A.M. van Hest: maikel.van.hest@nrel.gov

Joseph J. Berry: joe.berry@nrel.gov

ACKNOWLEDGMENTS

This work was started with seed funds from the Renewable and Sustainable Energy Institute (RASEI) at University of Colorado Boulder to support S.E.S and S.P.D, with support for S.P.D. to continue and complete the work provided first by the Oak Ridge Institute for Science and Education (ORISE) funded by the US Department of Energy (DOE) Solar Energy Technology Office (SETO) contract number DE-SC00014664 and then the Hybrid Perovskite Solar Cell (HPSC) Program funded SETO under Contract No. DE-AC36-08-GO28308 both at the National Renewable Energy Laboratory (NREL). D.T.M., T.R.K., and J.J.B. were supported by the HPSC

Program funded by SETO under DOE Contract No. DE-AC36-08-GO28308 with NREL. M.C.B. was supported by the DOE Solar Photo Chemistry program of the Office of Basic Energy Sciences, also under Contract No. DE-AC36-08-GO28308 with NREL. J.A.C. was funded by the DOE Office of Energy Efficiency and Renewable Energy (EERE) Postdoctoral Research Award under the EERE Solar Energy Technologies Office under DOE contract number DE-SC00014664. B.D., and M.F.A.M.v.H. were supported on this work by the US−India Partnership to Advance Clean Energy-Research (PACE- R) for the Solar Energy Research Institute for India and the United States (SERIIUS), funded jointly by the U.S. DOE (Office of Science, Office of Basic Energy Sciences, and Energy Efficiency and Renewable Energy, Solar Energy Technology Program, also under subcontract DE-AC36- 08GO28308) as well as the Government of India, through the Department of Science and Technology under Subcontract IUSSTF/JCERDC-SERIIUS/2012 dated 22 November 2012. D.M.F. was supported by the DOE, Office of Science, Office of Workforce Development for Teachers and Scientists, Office of Science Graduate Student Research (SCGSR) program under contract number DE-SC0014664.

REFERENCES

(1) Manser, J. S.; Christians, J. A.; Kamat, P. V. Intriguing Optoelectronic Properties of Metal Halide Perovskites. *Chem. Rev.* **2016**, *116* (21), 12956–13008.

(2) Green, M. A.; Ho-Baillie, A.; Snaith, H. J. The Emergence of Perovskite Solar Cells. *Nat. Photonics* **2014**, *8* (7), 506–514.

(3) Snaith, H. J. Perovskites: The Emergence of a New Era for Low-Cost, High-Efficiency Solar Cells. *J. Phys. Chem. Lett.* **2013**, *4* (21), 3623–3630.

(4) Li, Z.; Yang, M.; Park, J. S.; Wei, S. H.; Berry, J. J.; Zhu, K. Stabilizing Perovskite Structures by Tuning Tolerance Factor: Formation of Formamidinium and Cesium Lead

Iodide Solid-State Alloys. *Chem. Mater.* **2016**, *28* (1), 284–292.

(5) Kojima, A.; Teshima, K.; Shirai, Y.; and Teshima, M. Organometal Halide Perovskites as Visible- Light Sensitizers for Photovoltaic Cells. *J Am Chem Soc* **2009**, *131* (October), 6050–6051.

(6) Yang, W. S.; Park, B.; Jung, E. H.; Jeon, N. J. Iodide Management in Formamidinium-Lead-Halide – Based Perovskite Layers for Efficient Solar Cells. *Science* **2017**, *356* (June), 1376–1379.

(7) Aguiar, J. A.; Wozny, S.; Holesinger, T. G.; Aoki, T.; Patel, M. K.; Yang, M.; Berry, J. J.; Al-Jassim, M.; Zhou, W.; Zhu, K. In Situ Investigation of the Formation and Metastability of Formamidinium Lead Tri-Iodide Perovskite Solar Cells. *Energy Environ. Sci.* **2016**, *9*(7), 2372–2382.

(8) Aguiar, J. A.; Wozny, S.; Alkurd, N. R.; Yang, M.; Kovarik, L.; Holesinger, T. G.; Al-Jassim, M.; Zhu, K.; Zhou, W.; Berry, J. J. Effect of Water Vapor, Temperature, and Rapid Annealing on Formamidinium Lead Triiodide Perovskite Crystallization. *ACS Energy Lett.* **2016**, *1* (1), 155–161.

(9) Miller, E. M.; Zhao, Y.; Mercado, C. C.; Saha, S. K.; Luther, J. M.; Zhu, K.; Stevanović, V.; Perkins, C. L.; van de Lagemaat, J. Substrate-Controlled Band Positions in $CH_3NH_3PbI_3$ Perovskite Films. *Phys. Chem. Chem. Phys.* **2014**, *16* (40), 22122–22130.

(10) Zhao, Y.; Zhu, K. Organic–inorganic Hybrid Lead Halide Perovskites for Optoelectronic and Electronic Applications. *Chem. Soc. Rev.* **2016**, *45* (3), 655–689.

(11) Kim, D. H.; Park, J.; Li, Z.; Yang, M.; Park, J. S.; Park, I. J.; Kim, J. Y.; Berry, J. J.; Rumbles, G.; Zhu, K. 300% Enhancement of Carrier Mobility in Uniaxial-Oriented Perovskite Films Formed by Topotactic-Oriented Attachment. *Adv. Mater.* **2017**, *29* (23),

1–8.

(12) Steirer, K. X.; Schulz, P.; Teeter, G.; Stevanovic, V.; Yang, M.; Zhu, K.; Berry, J. J. Defect Tolerance in Methylammonium Lead Triiodide Perovskite. *ACS Energy Lett.* **2016**, *1* (2), 360–366.

(13) Sanehira, E. M.; Tremolet De Villers, B. J.; Schulz, P.; Reese, M. O.; Ferrere, S.; Zhu, K.; Lin, L. Y.; Berry, J. J.; Luther, J. M. Influence of Electrode Interfaces on the Stability of Perovskite Solar Cells: Reduced Degradation Using MoO_x/Al for Hole Collection. *ACS Energy Lett.* **2016**, *1* (1), 38–45.

(14) Christians, J. A.; Schulz, P.; Tinkham, J. S.; Schloemer, T. H.; Harvey, S. P.; Tremolet de Villers, B. J.; Sellinger, A.; Berry, J. J.; Luther, J. M. Tailored Interfaces of Unencapsulated Perovskite Solar Cells for >1,000 Hour Operational Stability. *Nat. Energy* **2018**, *3* (1), 68–74.

(15) Yang, M.; Li, Z.; Reese, M. O.; Reid, O. G.; Kim, D. H.; Siol, S.; Klein, T. R.; Yan, Y.; Berry, J. J.; Van Hest, M. F. A. M.; et al. Perovskite Ink with Wide Processing Window for Scalable High-Efficiency Solar Cells. *Nat. Energy* **2017**, *2* (5), 1–9.

(16) Noel, N. K.; Habisreutinger, S. N.; Wenger, B.; Klug, M. T.; Hörantner, M. T.; Johnston, M. B.; Nicholas, R. J.; Moore, D. T.; Snaith, H. J. A Low Viscosity, Low Boiling Point, Clean Solvent System for the Rapid Crystallisation of Highly Specular Perovskite Films. *Energy Environ. Sci.* **2017**, *10* (1), 145–152.

(17) Song, T.-B.; Chen, Q.; Zhou, H.; Jiang, C.; Wang, H.-H.; (Michael) Yang, Y.; Liu, Y.; You, J.; Yang, Y. Perovskite Solar Cells: Film Formation and Properties. *J. Mater. Chem. A* **2015**, *3* (17), 9032–9050.

(18) Li, T.; Dunlap-Shohl, W. A.; Han, Q.; Mitzi, D. B. Melt Processing of Hybrid Organic-

Inorganic Lead Iodide Layered Perovskites. *Chem. Mater.* **2017**, *29* (15), 6200–6204.

(19) Bi, C.; Chen, B.; Wei, H.; DeLuca, S.; Huang, J. Efficient Flexible Solar Cell Based on Composition-Tailored Hybrid Perovskite. *Adv. Mater.* **2017**, *29* (30), 1–6.

(20) Zhang, F.; Song, J.; Chen, M.; Liu, J.; Hao, Y.; Wang, Y.; Qu, J.; Zeng, P. Enhanced Perovskite Morphology and Crystallinity for High Performance Perovskite Solar Cells Using a Porous Hole Transport Layer from Polystyrene Nanospheres. *Phys. Chem. Chem. Phys.* **2016**, *18* (48), 32903–32909.

(21) Dou, B.; Miller, E. M.; Christians, J. A.; Sanehira, E. M.; Klein, T. R.; Barnes, F. S.; Shaheen, S. E.; Garner, S. M.; Ghosh, S.; Mallick, A.; et al. High-Performance Flexible Perovskite Solar Cells on Ultrathin Glass: Implications of the TCO. *J. Phys. Chem. Lett.***2017**, *8* (19), 4960–4966.

(22) Dualeh, A.; Tétreault, N.; Moehl, T.; Gao, P.; Nazeeruddin, M. K.; Grätzel, M. Effect of Annealing Temperature on Film Morphology of Organic-Inorganic Hybrid Pervoskite Solid-State Solar Cells. *Adv. Funct. Mater.* **2014**, *24* (21), 3250–3258.

(23) Nenon, D. P.; Christians, J. A.; Wheeler, L. M.; Blackburn, J. L.; Sanehira, E. M.; Dou, B.; Olsen, M. L.; Zhu, K.; Berry, J. J.; Luther, J. M. Structural and Chemical Evolution of Methylammonium Lead Halide Perovskites during Thermal Processing from Solution. *Energy Environ. Sci.* **2016**, *9* (6), 2072–2082.

(24) Hooper, K. E. A.; Lee, H. K. H.; Newman, M. J.; Meroni, S.; Baker, J.; Watson, T. M.; Tsoi, W. C. Probing the Degradation and Homogeneity of Embedded Perovskite Semiconducting Layers in Photovoltaic Devices by Raman Spectroscopy. *Phys. Chem. Chem. Phys.* **2017**, *19* (7), 5246–5253.

(25) Niu, G.; Guo, X.; Wang, L. Review of Recent Progress in Chemical Stability of

Perovskite Solar Cells. *J. Mater. Chem. A*__2015__, *3* (17), 8970–8980.

(26) Philippe, B.; Park, B. W.; Lindblad, R.; Oscarsson, J.; Ahmadi, S.; Johansson, E. M. J.; Rensmo, H. Chemical and Electronic Structure Characterization of Lead Halide Perovskites and Stability Behavior under Different Exposures-A Photoelectron Spectroscopy Investigation. *Chem. Mater.* **2015**, *27* (5), 1720–1731.

(27) Sadhanala, A.; Deschler, F.; Thomas, T. H.; Dutton, S. E.; Goedel, K. C.; Hanusch, F. C.; Lai, M. L.; Steiner, U.; Bein, T.; Docampo, P.; et al. Preparation of Single-Phase Films of $CH_3NH_3Pb(I_{1-x}Br_x)_3$ with Sharp Optical Band Edges. *J. Phys. Chem. Lett.* **2014**, *5* (15), 2501–2505.

(28) Makuta, S.; Liu, M.; Endo, M.; Nishimura, H.; Wakamiya, A.; Tachibana, Y. Photo-Excitation Intensity Dependent Electron and Hole Injections from Lead Iodide Perovskite to Nanocrystalline TiO_2 and Spiro-OMeTAD. *Chem. Commun.* **2016**, *52* (4), 673–676.

(29) Yang, Y.; Ostrowski, D. P.; France, R. M.; Zhu, K.; Van De Lagemaat, J.; Luther, J. M.; Beard, M. C. Observation of a Hot-Phonon Bottleneck in Lead-Iodide Perovskites. *Nat. Photonics* **2016**, *10* (1), 53–59.

(30) Xing, G.; Wu, B.; Wu, X.; Li, M.; Du, B.; Wei, Q.; Guo, J.; Yeow, E. K. L.; Sum, T. C.; Huang, W. Transcending the Slow Bimolecular Recombination in Lead-Halide Perovskites for Electroluminescence. *Nat. Commun.* **2017**, *8,* 14558.

(31) Szafrański, M.; Katrusiak, A. Mechanism of Pressure-Induced Phase Transitions, Amorphization, and Absorption-Edge Shift in Photovoltaic Methylammonium Lead Iodide. *J. Phys. Chem. Lett.* **2016**, 7 (17), 3458–3466.

(32) Zhao, J.; Deng, Y.; Wei, H.; Zheng, X.; Yu, Z.; Shao, Y.; Shield, J. E.; Huang, J. Strained Hybrid Perovskite Thin Films and Their Impact on the Intrinsic Stability of Perovskite

Solar Cells. 2017, No. November.

(33) Yang, M.; Zhou, Y.; Zeng, Y.; Jiang, C. S.; Padture, N. P.; Zhu, K. Square-Centimeter Solution-Processed Planar $CH_3NH_3PbI_3$ Perovskite Solar Cells with Efficiency Exceeding 15%. *Adv. Mater.* **2015**, *27* (41), 6363–6370.

(34) Burschka, J.; Pellet, N.; Moon, S. J.; Humphry-Baker, R.; Gao, P.; Nazeeruddin, M. K.; Grätzel, M. Sequential Deposition as a Route to High-Performance Perovskite-Sensitized Solar Cells. *Nature* **2013**, *499* (7458), 316–319.

(35) Yang, M.; Zhang, T.; Schulz, P.; Li, Z.; Li, G.; Kim, D. H.; Guo, N.; Berry, J. J.; Zhu, K.; Zhao, Y. Facile Fabrication of Large-Grain $CH_3NH_3PbI_{3-x}Br_x$ Films for High-Efficiency Solar Cells via CH_3NH_3Br-Selective Ostwald Ripening. *Nat. Commun.* **2016**, *7* (May), 12305.